Soft Matter

PAPER

Cite this: *Soft Matter*, 2019, **15**, 1335

Triggered disassembly and reassembly of actin networks induces rigidity phase transitions†

Bekele J. Gurmessa,[a] Nicholas Bitten,[b] Dan T. Nguyen,[c] Omar A. Saleh,[c] Jennifer L. Ross,[d] Moumita Das[b] and Rae M. Robertson-Anderson *[a]

Received 19th September 2018,
Accepted 4th December 2018

DOI: 10.1039/c8sm01912f

rsc.li/soft-matter-journal

Non-equilibrium soft materials, such as networks of actin proteins, have been intensely investigated over the past decade due to their promise for designing smart materials and understanding cell mechanics. However, current methods are unable to measure the time-dependent mechanics of such systems or map mechanics to the corresponding dynamic macromolecular properties. Here, we present an experimental approach that combines time-resolved optical tweezers microrheology with diffusion-controlled microfluidics to measure the time-evolution of microscale mechanical properties of dynamic systems during triggered activity. We use these methods to measure the viscoelastic moduli of entangled and crosslinked actin networks during chemically-triggered depolymerization and repolymerization of actin filaments. During disassembly, we find that the moduli exhibit two distinct exponential decays, with experimental time constants of ~169 min and ~47 min. Conversely, during reassembly, measured moduli initially exhibit power-law increase with time, after which steady-state values are achieved. We develop toy mathematical models that couple the time-evolution of filament lengths with rigidity percolation theory to shed light onto the molecular mechanisms underlying the observed mechanical transitions. The models suggest that these two distinct behaviors both arise from phase transitions between a rigidly percolated network and a non-rigid regime. Our approach and collective results can inform the general principles underlying the mechanics of a large class of dynamic, non-equilibrium systems and materials of current interest.

1 Introduction

The cell cytoskeleton is one of the most widely studied non-equilibrium materials in existence due to the principal role it plays in orchestrating mechanical processes such as mitosis, crawling, and apoptosis.[1–4] To actively regulate the mechanical properties of the cytoskeleton, networks of actin proteins continuously disassemble, reassemble, and reorganize by actin transitioning between filamentous and monomeric states. As such, actin networks have been intensely studied as a platform for creating dynamic and reconfigurable materials. However, determining how the mechanics of actin networks evolve during disassembly and reassembly remains elusive. Previous studies have focused on measuring either the mechanical properties of steady-state actin networks or the polymerization kinetics of single actin filaments. Yet, how de/repolymerization kinetics of single actin filaments map to time-varying mechanical properties of actively evolving networks remains an open question. The principal reason for this lack of understanding stems from a dearth of techniques to simultaneously trigger activity and measure non-equilibrium mechanics of dense viscoelastic networks.[5,6]

In the presence of ATP and magnesium, globular actin monomers (G-actin) polymerize into semiflexible filaments (F-actin) with persistence lengths of ~10 μm and typical contour lengths of ~1–50 μm.[7–9] Polymerization proceeds *via* slow nucleation, in which stable trimers are formed, followed by elongation, in which single monomers bind sequentially to the end of the growing filament. The rate constant for elongation is generally accepted to be ~11.6 μM^{-1} s^{-1}, however values as low as ~1.5 μM^{-1} s^{-1} have been reported.[10–15] For a single filament, the rate of polymerization is solely dependent on the pool of free monomers, slowing as the pool is depleted. However, for concentrated networks of filaments, other factors such as competition between trimers, filament annealing, and fragmentation have been suggested to be important to accurately describing the time course of polymerization.[15–17]

Depletion of ATP, introduction of calcium, and/or depletion of free G-actin causes F-actin to depolymerize;[18,19] and experimentally measured depolymerization rates of 0.2–0.9 s^{-1} have been reported.[11,13,14,20] The age of the filament has also been

[a] *Department of Physics and Biophysics, University of San Diego, San Diego, USA. E-mail: randerson@sandiego.edu*
[b] *School of Physics and Astronomy, Rochester Institute of Technology, Rochester, USA*
[c] *Department of Materials & BMSE Program, University of California, Santa Barbara, USA*
[d] *Department of Physics, University of Massachusetts, Amherst, USA*

† Electronic supplementary information (ESI) available. See DOI: 10.1039/c8sm01912f

suggested to play a role in depolymerization, with filaments aged beyond ~5–10 min, transitioning from fast (1.8 s^{-1}) to slow (0.1–0.2 s^{-1}) depolymerization.[11,21,22]

High concentrations of F-actin form entangled networks which can also be crosslinked in the presence of actin-binding proteins, leading to unique viscoelastic mechanical properties. Motivated, in part, by the relevance to cellular mechanics, the viscoelastic response of steady-state entangled and crosslinked actin networks have been extensively studied.[23–29] The majority of studies have focused on characterizing the frequency-dependent storage and loss moduli ($G'(\omega)$ and $G''(\omega)$), which quantify the relative elasticity ($G'(\omega)$) and fluidity ($G''(\omega)$) of the system.[26,30–33] However, relatively little is known regarding how these properties evolve with time as networks disassemble and reassemble.[23,34]

Here, we couple time-resolved active microrheology with a recently developed microfluidic platform to measure the time trajectories of local viscoelastic moduli of entangled and crosslinked actin networks during dynamic disassembly and subsequent reassembly. Specifically, we chemically trigger actin depolymerization and subsequent repolymerization while simultaneously measuring the force exerted by the network to resist microscale oscillations of an optically trapped microsphere over the time course of disassembly and reassembly (Fig. 1). To qualitatively understand our results, we develop toy mathematical models that integrate polymerization kinetics of actin filaments with the mechanical rigidity of actin networks to describe how the storage modulus of the network varies in time during depolymerization and repolymerization. Polymerization kinetics are modeled using a Master equation approach,[15,35–38] and the mechanics of the network are characterized using an Effective Medium Theory of rigidity percolation.[39–42] Our approach and results shed much needed new light on the time-varying mechanics of the cytoskeleton and the underlying principles of other active, self-assembling systems of current interest.

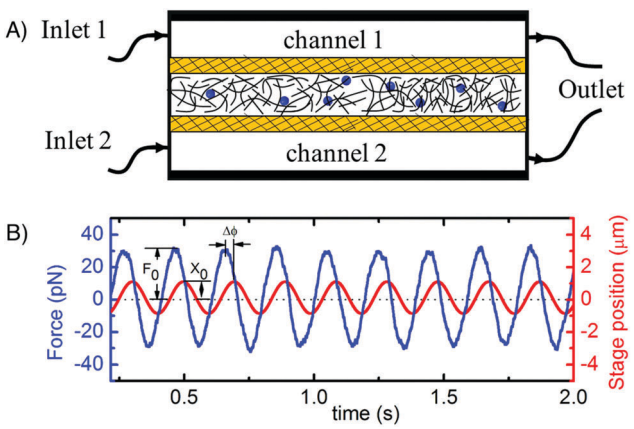

Fig. 1 Schematic of experimental approach. (A) Illustration of microfluidic device comprised of a central channel that contains the actin sample (black) and microspheres (blue), two flanking channels used for buffer exchange (through inlets 1 & 2 and an outlet), and two semipermeable membranes (brown) that separate the channels. (B) Sample microrheology data showing bead position (red) and force (blue) as a function of time. The amplitude of the force F_0 and position X_0 as well as the phase shift $\Delta\phi$ between the force and position are used to determine viscoelastic moduli G' and G''. Data shown is for an oscillation frequency of ω = 32 rad s^{-1}.

2 Materials and methods

Sample preparation

G-actin (Cytoskeleton, Inc) is stored at −80 °C in G-buffer [2 mM Tris pH 8.0, 0.5 mM DTT, 0.1 mM $CaCl_2$]. The presence of calcium and lack of ATP suppresses polymerization so actin remains in monomeric form. Entangled F-actin solutions were assembled in the microfluidic sample chamber (described below) by polymerizing 11.6 μM G-actin in F-buffer [10 mM Imidazole pH 7.0, 50 mM KCl, 1 mM $MgCl_2$, 1 mM EGTA, 0.4 mM ATP] for 1 hour at room temperature, as described previously.[43,44] The magnesium, potassium and ATP in F-buffer promote polymerization. Crosslinked networks were prepared similarly but 1.6 μM of G-actin was biotinylated and NeutrAvidin was added at a molar ratio of 0.07 to actin monomers, as described previously.[43]

To measure the length distribution of actin filaments in networks, actin filaments were labeled with Alexa-568 and imaged using an A1R Nikon laser scanning confocal microscope with 60× 1.4 NA objective and QImaging CCD camera, as described previously.[44–46] Briefly, 512 × 512 images were taken on the surface of the sample chamber and only filaments that were adhered to the surface (visibly immobile) were measured. To determine the length distribution, the lengths of 377 actin filaments were measured using the freehand tool in Fiji (Fig. 2). We find that actin filament lengths in both networks are gamma distributed with a mode of 5.1 μm, mean of 7.2 μm and standard deviation of 4.0 μm (Fig. 2).

The mesh size for both networks is ξ = 0.42 μm ($0.3/\sqrt{c_a}$, with c_a being the actin concentration in mg ml^{-1}),[47] and the length between entanglements is l_e ~ 0.89 μm.[45] The average length between crosslinks for crosslinked networks is l_c ~ 0.1 μm,[43] so every filament entanglement or crossing can be assumed to be permanently linked by crosslinkers. For microrheology measurements, a trace amount of BSA-coated microspheres (4.5 μm diameter) were added to samples prior to polymerization.[48] The bead size was chosen such that it can probe the continuum network mechanics rather than the local network structure. Previous work has shown that a microsphere size of ~$3l_e$ is sufficient to yield continuum mechanics for entangled polymer solutions,[49,50] and our previous studies on similar actin networks have also used this bead size and reported continuum behavior.[43–45]

Microfluidics

The construction of the microfluidic devices, based on the techniques presented in ref. 51, is thoroughly described in Appendix A. As shown in Fig. 1, the device has a central sample channel that is bordered on top and bottom by two semipermeable membranes and flanking buffer channels. The left and right sides of the sample chamber are sealed with epoxy so the sample is completely enclosed within the central chamber. Tubing inserted into both ends of the flanking buffer channels

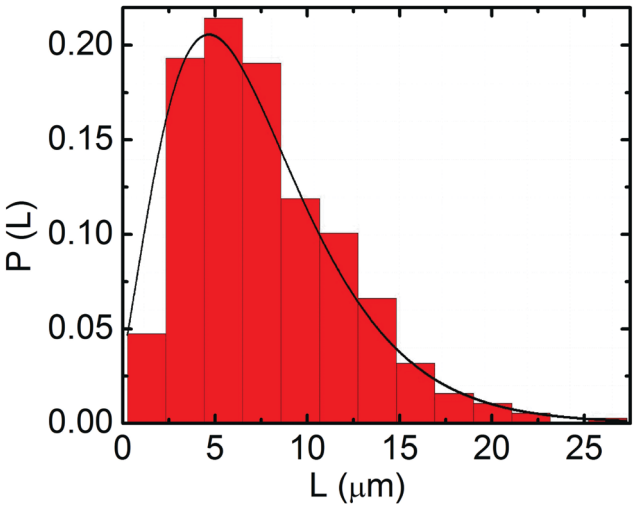

Fig. 2 Probability distribution of actin filament lengths measured for a steady-state fully percolated network. The distribution shows the measured lengths of 377 actin filaments in the network, as described in Methods. The distribution is well fit to a gamma distribution with a mean of 7.2 μm, mode of 5.1 μm, standard deviation of 4.0 μm, and shape and scale parameters of 3.25 and 2.24 μm. The 12 lengths corresponding to the 12 bars in the histogram are used in the mathematical model to obtain predictions of the mechanical response during network disassembly.

enables buffer exchange within the sample chamber *via* passive diffusion through the membranes rather than directed flow.

For microrheology measurements, the actin solution was pipetted into the central channel and the flanking channels were filled with F-buffer (which promotes polymerization of G-actin and enables F-actin to maintain its polymerization state). To trigger F-actin disassembly, existing F-buffer is pulled from the flanking channels at a flow rate of 5 μl min^{-1}, using a digitally-controlled syringe pump, as G-buffer (which triggers filament depolymerization) is pulled in. The result is diffusion-controlled exchange of F-buffer with G-buffer in the central sample channel. Complete buffer exchange is achieved in ~6–7 min.[51,52] To actuate network reassembly, *via* actin repolymerization, G-buffer in the flanking channels is exchanged with F-buffer.

Microrheology

We use an optical trap setup built by outfitting an Olympus IX71 fluorescence microscope with a 1064 nm ND:YAG fiber laser (Manlight) focused with a 60× 1.4 NA objective, as described and validated previously.[45,50] Following microfluidic triggering, a microsphere embedded in the sample is trapped and oscillated sinusoidally relative to the sample at an amplitude of 1 μm at five frequencies from ω = 0.5 rad s^{-1} to ω = 107 rad s^{-1} using a piezoelectric nanopositioning stage (Mad City Laboratories) (Fig. 1). A position-sensing detector (Pacific Silicon Sensors) is used to measure the laser deflection, which is proportional to the force on the bead from the surrounding network. The trap stiffness was calibrated *via* Stokes drag in water[53] and passive equipartition methods.[28] We fit both the stage position and force data to sine curves using the least squares method, and calculate the storage modulus $G'(\omega)$ and loss modulus $G''(\omega)$ *via* $G'(\omega) = |F_0|\cos(\Delta\phi)/6\pi a|X_0|$ and $G''(\omega) = |F_0|\sin(\Delta\phi)/6\pi a|X_0|$ where F_0, X_0, $\Delta\phi$, and a are the force amplitude, stage position amplitude, phase shift between the force and stage position, and bead radius, respectively.[26,50,54] We carried out measurements every 5 min over the time course of disassembly and reassembly with t = 0 being immediately before buffer exchange is initiated. The initial data point for reassembly occurs ~10 min after the final time point of disassembly due to the time needed to switch reservoirs and initiate buffer exchange. While chemical triggering *via* buffer exchange requires ~6–7 minutes to complete, subsequent micrheology measurements take only a few seconds to perform, so this technique can resolve changes in mechanics that occur as fast as within several seconds.

Mathematical model

To theoretically obtain the mechanical response of the network as a function of time, we use an integrated approach where we first use Master equations to calculate the average filament length of the network $\langle L\rangle$ as a function of time, and then use Rigidity Percolation theory to obtain the linear storage modulus G' as a function of $\langle L\rangle$. We use these results to obtain G' as a function of time, for both the disassembling and the reassembling network. Below, we summarize our mathematical model and method, which is fully described in Appendix B.

Master equations for filament length. We study the time evolution of the concentration of filaments of length L, under the influence of microscopic processes that lead to the growth or shrinkage of actin filaments, using a Master equation framework. For depolymerization, we consider a spatially homogeneous system with a fixed amount of actin, initially present in the form of filaments of a given length in a network. Assuming that the filaments depolymerize independent of each other, we obtain the probability, $P(L,t)$, that a filament has length L at time t, for a given depolymerization rate, by solving the Master equation for disassembly described in Appendix B. We assume that the polymerization rate is negligibly small during this stage. The probability $P(L,t)$ is then used to calculate the average filament length at a given time t, $\langle L\rangle = \Sigma LP(L,t)$. We perform calculations for twelve different initial filament lengths that correspond to the full distribution of experimentally measured lengths (Fig. 2). We assume a depolymerization rate of 0.22 s^{-1} based off of values reported in the literature.[13] In converting average filament length from monomers to μm, we assume that each monomer is 2.7 nm long.[7,44,55] We do not explicitly take into account interactions with the surrounding solvent.

The Master equation for filament reassembly, on the other hand, is a more complex multi-stage nucleation–elongation process, which we model as a five-stage phenomenon following ref. 15 as described in Appendix B. We assume that at the beginning of reassembly, actin is present only in the form of monomers which get depleted as more and more filaments are formed. The polymerization rate therefore depends on the monomer concentration $m(t)$ at any given time t as $k_+m(t)$. Additionally, the initial nucleation stage of an actin filament is experimentally known to be kinetically unfavorable,[56,57] and so in this stage we

assume a depolymerization rate k_{-1} that is comparable to the polymerization rate.[15] As the size of the oligomer grows this depolymerization rate decreases, *i.e.* a dimer depolymerizes at a faster rate than a trimer, with $k_{-1} > k_{-2}$. Following ref. 13 the depolymerization rates of larger oligomers, k_{-3} and k_{-4}, are set to 10 s^{-1} and 0 s^{-1}, respectively. The depolymerization rate of oligomers of size greater than or equal to 5 monomers is assumed to be 1 s^{-1}. The polymerization rate for all steps is assumed to be the experimentally measured value of 10 μM^{-1} s^{-1} as used in ref. 10 and 13. The probability $P(L,t)$ during the filament reassembly phase is obtained by solving the corresponding Master equation as described in Appendix B, and is used to calculate the average filament length $\langle L \rangle$ as in the case of filament disassembly.

Rigidity percolation theory

The rigidity percolation theory models a biopolymer network as a disordered network made of fibers, and consisting of both flexible (sparsely connected) and rigid (densely connected) regions. When flexible regions span the network, external strains can be accommodated without stretching or bending the fibers. As a result, the entire network is flexible, does not resist external strains, and has a zero storage modulus. On the other hand, when the rigid regions percolate, the network becomes mechanically rigid, and has a non-zero storage modulus. The system therefore goes from non-rigid to rigid at a certain number density of fibers known as the rigidity percolation threshold, and this mechanical phase transition is known as the rigidity percolation transition. Within the rigid phase, there are two mechanical regimes: an affinely deforming regime corresponding to a dense, rigid network that deforms uniformly at all length scales and has a storage modulus that decreases very slowly with fiber content; and a floppy, barely-rigid network that deforms non-uniformly or non-affinely at different length scales with large variations in the storage modulus with small variations in fiber content.[39] Details of this model are described in Appendix B. The storage modulus of the network G' for a given average fiber length $\langle L \rangle$ is obtained by means of an effective medium theory calculation.[39,40]

3 Results and discussion

We designed our experimental approach to enable simultaneous triggering and measurement of mechanical activity in a wide range of non-equilibrium soft materials, complex fluids, and macromolecular networks including expensive, difficult to produce, and fragile systems. To actuate activity, we use microfluidic perfusion chambers to modulate the chemical environment of the system while preventing directional flow, disruption, or loss of sample. We use microrheology rather than macrorheology to enable the use of microliter sample sizes, and the ability to apply repeated perturbations over time without disrupting or modifying the network. This method is accessible to delicate and valuable systems, and ensures that the time-dependent network architecture is not altered by the repeated straining.[58,59] To perform well-separated time-dependent measurements that can be time-resolved on the scale of seconds, we use active microrheology rather than passive methods that rely on the time-trajectories of passively diffusing beads to extract viscoelastic moduli. The actin network assembly dynamics we investigate here occurs over the timescale of minutes to hours; however, our approach can resolve mechanical changes that occur as fast as several seconds.

We use this approach to measure the storage and loss moduli, $G'(\omega)$ and $G''(\omega)$, of entangled and crosslinked actin networks as a function of time during chemically-triggered depolymerization and subsequent repolymerization of actin filaments. We focus our discussion on the time evolution of $G'(\omega)$, as it is a better indicator of network formation than $G''(\omega)$. Fig. 3 shows the storage moduli measured during induced depolymerization (Fig. 3A) and subsequent repolymerization (Fig. 3B) of actin filaments in entangled and crosslinked networks. We normalize $G'(\omega)$ by the corresponding steady-state network value, $G_0'(\omega)$, and for each time point, display the maximum and minimum measured values as well as the value averaged over all frequencies. As shown, G'/G_0' for both networks and all measured frequencies collapse to a single master curve. This result suggests that the molecular mechanisms driving self-assembly of actin networks depend on permanent crossings between filaments, but may not distinguish between physical and chemical links.

In both entangled and crosslinked networks, the mesh size and length between entanglements is the same, so it is possible that changing these parameters could influence our results. We discuss this potential influence below. While outside the scope of the current manuscript, in future work we plan to test the effect of these parameters directly by carrying out experiments at different actin and crosslinker concentrations (effectively varying ξ, l_e, and l_c).

During depolymerization, the time-evolution of the storage modulus displays two distinct regimes – a fast and slow regime – which each exhibit apparent exponential decay with time (Fig. 3A). The initial slow decay phase persists until $t \sim 90$ min, and fits well to an exponential with a time constant of $\tau_1 = 169 \pm 13$ min. The second decay phase, which takes over at $t \sim 90$ min, is described by a much faster time constant of $\tau_2 = 47 \pm 2$ min. Not only does the data in each phase appear to be well described by an exponential, the choice of exponentials for fitting was further motivated by the fact that standard single-process relaxations in nature are most often described by exponentials with time constants that correlate to the characteristic timescale for the decay mechanism. We discuss the underlying mechanism for this process below.

In contrast, during reassembly, G'/G_0' curves are well fit to a power-law increase with time for $t < 90$ min, with scaling exponent $\alpha = 1.1 \pm 0.09$, after which they reach steady-state values (Fig. 3B). G'/G_0' curves during reassembly likely follow power-law rather than exponential increase, as the processes for reassembly are more complex than for disassembly, as we describe further below. While G'/G_0' values are relatively constant ($\alpha \sim 0$) for $t > 90$ min, upon close inspection a slight dip in G'/G_0' can be observed following saturation. We discuss the origin of this decrease below. While the reassembly process

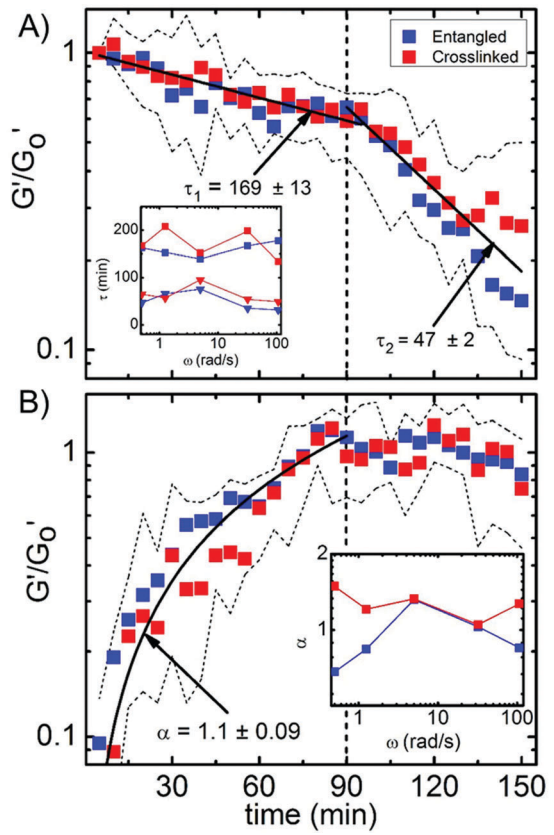

Fig. 3 Time course of storage modulus G' for actin networks during (A) disassembly and (B) reassembly. All G' values are normalized by the corresponding steady-state network value G_0'. The two dashed lines correspond to the maximum (top) and minimum (bottom) measured values among measurements taken at 5 different frequencies in the range ω = 0.5–107 rad s^{-1}. Red and blue points are G' values averaged over all frequencies for entangled (blue) and crosslinked (red) networks. Solid black lines are fits to the data corresponding to: (A) single exponential decays with time constants of $\tau_1 \sim 169 \pm 13$ min for $t < 90$ min and $\tau_2 \sim 47 \pm 2$ min for $t > 90$ min; (B) power-law scaling with exponent of $\alpha = 1.1 \pm 0.09$ for $t < 90$ min. Insets show: (A) the time constants for $t < 90$ min (squares) and $t > 90$ min (triangles), and (B) scaling exponents for $t < 90$ min, measured for each frequency and each network type. Dashed vertical lines correspond to the observed crossover time (90 min) between the first and second phases.

is relatively fast (~90 min) compared to disassembly (~150 min), the time needed to reach effectively complete reassembly is nearly identical to the time needed to switch to fast decay during disassembly. As we discuss further below, this reversible crossover timescale is likely the timescale at which a fully percolated network is achieved or destroyed.

To verify that the systems are fully disassembling and reassembling we compare our measured values at the beginning and end of de/repolymerization to those of steady-state networks and solutions of monomers. As shown in Fig. S1 (ESI†), the moduli measured at the beginning and end of each process are in good agreement with those measured in steady-state. Our measured steady-state moduli values are also comparable to previously reported values,[26,31,33,60,61] further demonstrating the validity of our measurements.

To shed light onto the molecular processes that drive the time-dependent mechanical response, we developed toy mathematical models, detailed in Methods and Appendix B, that couple the polymerization kinetics of single filaments to the formation and destruction of a rigidly percolated network.

For disassembly, we used a Master equation approach on twelve different experimentally measured initial filament lengths: 1.2 μm, 3.2 μm, 5.1 μm, 7.1 μm, 9.0 μm, 11.0 μm, 13.0 μm, 15.0 μm, 16.9 μm, 18.8 μm, 20.8 μm, and 24.7 μm (Fig. 2). We obtained the average filament length $\langle L \rangle$ as a function of time for each case, and then used rigidity percolation theory to map them to the corresponding storage modulus G'. As shown in Fig. 4A, our model predicts that the storage modulus G' initially decreases slowly with time before undergoing a distinct crossover to more rapid decay. The initial filament length plays the principal role in determining the timescale at which the transition takes place, as well as the steepness of the initial decay phase.

For an initial filament length of 5.1 μm, corresponding to the mode of the experimentally measured distribution of initial filament lengths (Fig. 2), the crossover time is ~83 min, quite close to our experimentally measured crossover time. While both experimental and theoretical results exhibit a crossover between two mechanical regimes, unlike experiments, theoretical curves do not exhibit simple exponential decay for each regime. Rather they exhibit near continuous curvature, especially at times <90 min (Fig. 4). Because of the simplistic nature of the model, we do not expect exact quantitative agreement between theoretical and experimental curves. In our model, the only process that contributes to decreasing the filament length during disassembly is depolymerization, which takes place at a constant rate. Furthermore, filaments depolymerize independently of one another. However, in experiments, filaments may disassemble at slightly different rates in a context dependent manner, *i.e.* based on their interaction with nearby filaments and potential fragmentation or annealing.[15,58] Further, it is possible that our experimental data actually contains higher modes that would lead to a smoother transition between phases, similar to that seen in theory curves, but the noise in the data masks these modes, resulting in only two apparent exponential phases.

Nonetheless, to further compare our predictions with experimental results, we fit the fast and slow regimes of each curve to exponential decays to extract approximate time constants for the slow and fast phases. As described above, disassembly arises solely from constant rate depolymerization of individual filaments in the model. As a result, for each of the two disassembly phases or regimes, we expect a single mode exponential decay. The time constants for the two disassembly regimes are however different. During the first regime when we have a dense, rigidly percolating network, the network deforms uniformly or affinely at all lengthscales, and G'/G_0' changes very slowly as the average filament length in the network decreases. This corresponds to a large decay timescale. During the second regime when the system is very close to the rigidity percolation transition, the network is very sparse and deforms non-affinely at different lengthscales. As a result, G'/G_0' changes very rapidly with small changes in average filament length in the network, giving rise to much smaller decay times.

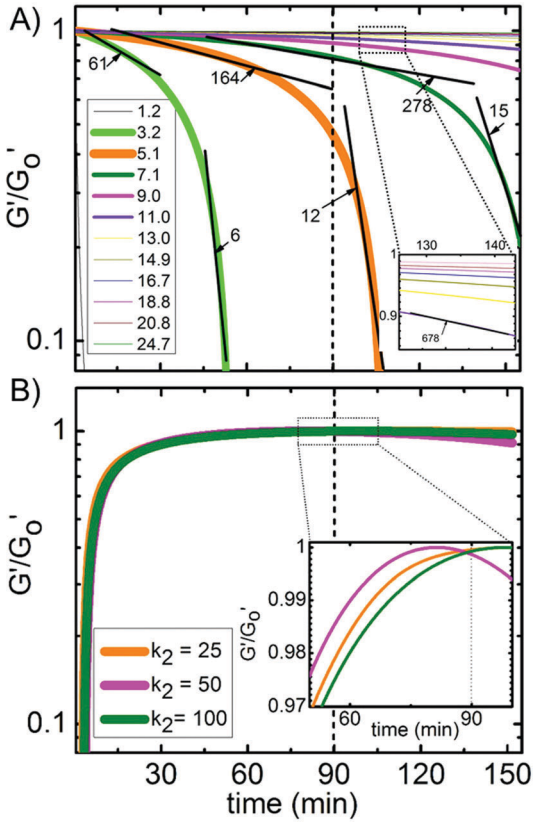

Fig. 4 Predicted storage modulus as a function of time during actin network (A) disassembly and (B) reassembly. Modulus values are normalized by the modulus value for a fully percolated network G_0'. (A) For disassembly, the displayed curves correspond to 12 different initial filament lengths corresponding to each of the measured filament lengths in the experimental length distribution (see Fig. 2). Lengths are listed in microns in the legend, and the width of the curves correspond to their probability in the length distribution. The straight lines show exponential fits for the mode length (5.1 μm, orange) and two adjacent lengths (3.2 μm, green; 7.1 μm, blue), with decay times displayed in minutes. The depolymerization rate is set to 0.22 s^{-1}. Inset shows a zoom-in of the curves for the longer length filaments (>9 μm) for t > 90 min. (B) For reassembly, displayed curves are results of the five-step model with varying trimer dissociation rates (k_{-2}) listed in s^{-1} in the legend. Dashed vertical lines correspond to the experimentally observed crossover time (90 min) between the first and second phases.

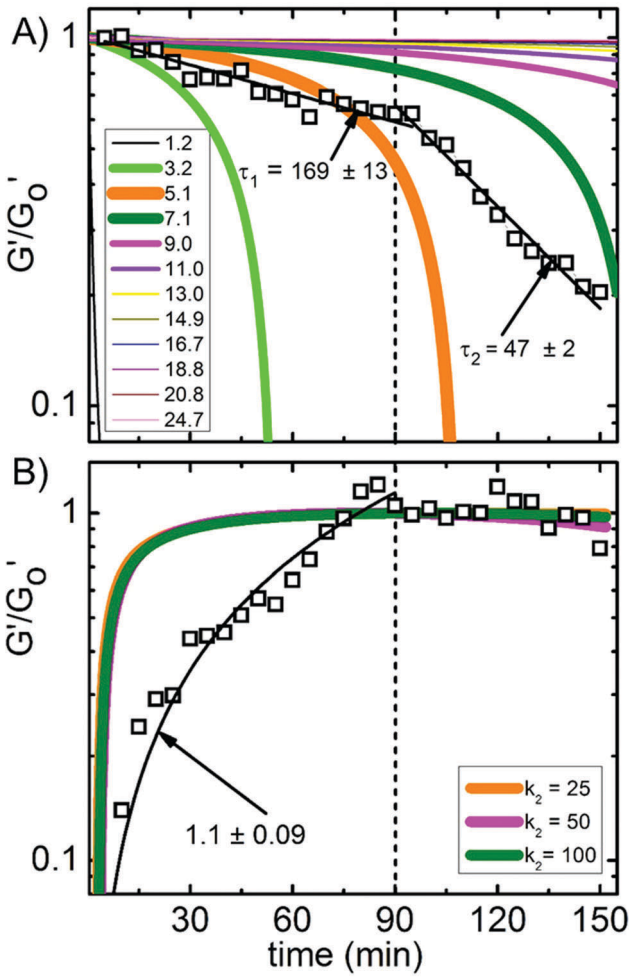

Fig. 5 Comparison of experimental and theoretical storage moduli as a function of time during network (A) disassembly and (B) reassembly. (A) Solid colored lines correspond to theoretical results for the 12 different experimentally measured filament lengths listed in microns in the legend. Open symbols correspond to the average experimentally measured modulus, and solid lines are exponential fits with decay times listed in minutes. (B) Solid colored lines correspond to theoretical results for 3 different trimer dissociation values, k_{-2}, listed in the legend in units of s^{-1}. Open symbols correspond to experimental values, and solid black lines show power law fit to the experimental results with the scaling exponent listed. Dashed vertical lines correspond to the observed crossover time (90 min) between the first and second phases.

For the mode initial filament length (5.1 μm), the decay time for the initial slow phase is ∼164 min, in excellent agreement with the experimentally measured time constant (Fig. 4A and 5A). Our predicted fast decay time constant for this mode length (τ_2 ∼ 12 min) is faster than the experimental value. However, as shown in Fig. 4A, the longer length filaments in the distribution do not reach the predicted crossover to fast decay until much later (>130 min). This theoretical result suggests that the second phase in our experimental measurements is a combination of slow decay from long filaments still in the rigid regime (as demonstrated by the 7.1 and 9.0 μm curves in Fig. 5A) and fast decay from shorter filaments. The long filaments slow the complete destruction of the network, and make the difference between slow and fast decay constants less extreme.

However, we do not expect the contributions from these longer filaments to influence the crossover time because the fraction of the distribution that these filaments comprise is still small compared to that of the mode length (5.1 μm). Because the transition in the model is so sharp, we expect the mode length to determine this crossover time as its contribution to the experimental curve is greatest. However, because there are so many very long filaments (∼9–25 μm) in the distribution, the second phase decay in experiments is much slower than in the theory due to the contributions from these long filaments still being in the first slow phase.

For reassembly, as described in the Methods and ESI,† we use a five-step model for nucleation–elongation[15] with a

polymerization rate similar to previously measured values.[10,13,15] We varied the dissociation rate for trimer formation k_{-2} (Fig. 4B), but fixed all other dissociation rates. As shown in Fig. 4B, our model predicts a crossover from non-affine to affine mechanical regimes, with G'/G_0' rapidly increasing for $\sim$20 min after which it slowly approaches steady-state values. The timescale at which the steady-state network value G_0' is reached is $\sim$90 min (Fig. 4B inset), in line with our experimental crossover time. The exact timescale at which full network formation occurs is weakly dependent on the value of k_{-2}.

The results of this simple model capture the biphasic evolution of G' seen in experiments, as well as the timescale to reach steady-state. They show that while the total actin density in our system stays the same, the distribution of filament lengths change dynamically with time. When the filaments are long enough to form networks that percolate sufficiently to be able to bear mechanical loads, we observe a crossover in the rigidity of the network.

Further, similar to experiments, our model also shows a slight dip in G'/G_0' following saturation for intermediate dissociation rates (k_{-2} = 50). We can understand this phenomenon as follows. In our model (and experiments), we have a finite monomer pool during filament assembly. The rate of polymerization depends on the concentration of available monomers, which decreases as polymerization proceeds. At the same time, during the early stages of filament assembly, the non-zero dissociation rate (k_{-2}) can release monomers back to the pool, making more monomers available for polymerization and thus increasing the polymerization rate. However, dissociation also decreases the net filament length. The subtle interplay between these competing processes is manifested in how varying the dissociation rate k_{-2} affects G'/G_0'. Once a system-spanning network has formed, the concentration of monomers in the pool is very small, and the polymerization rate is negligibly small. A small k_{-2} does not impact the polymerization process nor does it significantly decrease filament length, while a large k_{-2} slightly aids in the polymerization process by making more monomers available to the pool for polymerization. For both of these cases, the average filament length in the network continues to be large enough that the network remains densely linked and deforms completely affinely, which corresponds to the saturation of G'/G_0' observed in Fig. 4A and 5A. Conversely, for intermediate values of k_{-2} (k_{-2} = 50) dissociation does not appreciably increase the availability of monomers but it is sufficiently large to cause a small but noticeable decrease in the average filament length, leading to the dip in G'/G_0'.

Before the crossover, the functional form of the predicted G'/G_0' curves cannot quantitatively recapitulate the experimental results (Fig. 5B). As stated in the Introduction, it has recently been shown that the effect of competing nucleating centers can play a significant role in polymerization of dense networks.[17] Further, filament fragmentation and annealing have also been theoretically shown to impact polymerization kinetics of concentrated networks of filaments.[15] While outside the scope of the current manuscript, in future work we plan to incorporate these mechanisms into our model and achieve more quantitative agreement between experiment and theory.

We expect to observe power-law increase, as in experiments, because several processes, such as nucleation and elongation contribute to the change in filament length during reassembly. We expect that the power-law exponent will change if the processes that contribute to filament growth during reassembly, their associated timescales, or the separation of these timescales are very different from those used in our study. In the model, the multiple reassembly processes are incorporated by making reassembly a five-stage process with different polymerization and depolymerization rates for each stage. Furthermore, we assume a finite monomer pool; hence the polymerization rate is not constant and depends on the concentration of monomers, which decreases as polymerization proceeds. This interplay between multiple processes and timescales that are not necessarily well separated would lead to a power-law increase instead of an exponential one. The increase is much steeper in the model compared to experiments, because the model only takes filament nucleation and elongation into account, and ignores filament annealing and fragmentation.

We also expect that varying the density of filament crossings will cause the rigidity transition to shift in time. The transition to a rigid network will occur with fewer fully-formed filaments (shorter timescale) if the degree of filament crossing is substantially stronger (*i.e.* l_e or l_c is smaller). In future work, we plan to test this assumption directly by carrying out experiments at different actin and crosslinker concentrations (effectively varying l_e and l_c). In the rigid regime, more densely linked networks will deform more uniformly (or affinely) and hence G'/G_0' will vary more slowly. Therefore, in this regime, the time constant for the decay of G'/G_0' during disassembly will be larger, and the scaling exponent during reassembly will be smaller. Once the network starts losing rigidity, *i.e.* in the floppy regime, G'/G_0' changes rapidly and the dependence on filament crossings becomes negligibly small. In this regime, we do not expect to see a significant difference in the decay constants or scaling exponents as we vary l_e or l_c.

The stiffness of the filaments will also play a role in the mechanics. The rigidity percolation framework predicts that increasing the stiffness of the filaments will increase the magnitude of G'. However, as long as the filament type is the same (*i.e.* semiflexible filaments which cost energy to both stretch and bend), the transition from the rigid to non-rigid regime will take place at the same average filament length. This implies that, even if we change the filament stiffness, the time at which the transition takes place will remain unchanged. The time constants, on the other hand, which correspond to the rate at which G'/G_0' changes in the two regimes, will depend on filament stiffness. For stiffer filaments, we expect the network to deform in a more uniform manner, giving rise to a slower change in G'/G_0' (slower decay constants).

4 Conclusion

We have presented an experimental approach that combines time-resolved optical tweezers microrheology with diffusion-controlled

microfluidics, to measure the time-evolution of microscale mechanical properties of dynamic systems during triggered activity. We use this technique to measure the viscoelastic moduli of entangled and crosslinked actin networks during chemically-induced depolymerization and repolymerization of actin filaments. To inform our experimental results, we develop toy mathematical models that couple the time-evolution of filament lengths with rigidity percolation theory to predict the evolution of the storage modulus during network disassembly and reassembly. Our experiments show that the storage modulus exhibits two phases of behavior during both actin network disassembly and reassembly, with a distinct crossover at $\sim$90 min for both processes (Fig. 5). During disassembly, the modulus exhibits two distinct exponential decay phases. During reassembly, the modulus increases roughly linearly for the first $\sim$90 min after which a time-independent plateau is reached (Fig. 5). Our simple models show that this two-phase behavior arises from a rigidity percolation phase transition as the network is destroyed or reformed (Fig. 5). Our collective results fill a long-standing gap in knowledge regarding how polymerization kinetics of filamentous proteins map to time-varying mechanical properties of the network.

Further, our results provide insights into how cells can modulate their mechanical structure–function properties during the dynamic reorganization and remodeling of the cytoskeleton to facilitate cell shape change and movement. For example, our results are directly applicable to understanding the time-dependent mechanical properties of the lamellipodium at the leading edge of migrating cells,[1] the actin cortex during endocytosis,[62] and neutrophils during chemotaxis.[63] More generally, our work and results can inform the underlying principles of dynamic, self-assembling systems and materials. Finally, our techniques can be used to measure the time-dependent mechanical properties of the growing number of triggerable and reconfigurable materials currently under intense investigation.

Conflicts of interest

There are no conflicts to declare.

Appendix

A Microfluidics

The microfluidic device was fabricated as presented in ref. 51. Briefly, it consists of a cover slip (no. 0, 22 × 22 mm), a glass microscope slide, and a parafilm spacer. The cover slip, and glass slide were washed thoroughly with acetone, isopropanol, and deionized water (DI), then plasma cleaned. The slide, slip, and parafilm spacer were fused together using a soldering iron. The flow cell was then filled with a 50 : 1 mixture of poly (ethylene glycol) diacrylate (PEG-DA) and photoinitiator, 2-hydroxy-2-methyl-propiophenone (Sigma-Aldrich), diluted to 20% (v/v) in DI. The flow cell was exposed to UV through a custom photomask to form two semipermeable membranes of crosslinked PEG-DA then flushed with DI to remove the un-linked PEG-DA solution. This results in a central channel for holding the sample separated by semipermeable membranes from two flanking channels to enable buffer exchange *via* diffusion. The sample was pipetted into the central channel and the flanking channels were initially filled with F-buffer. Flanking channels were then connected to capillary tubes (74/95 μm inner/outer diameter, Paradigm Optics) at both ends. Both tubes from one end were connected to Tygon tubing I (Cole Parmer Tygon tubing AAD02103-CP, 0.020/0.060 inches inner/outer diameter), while the other ends were connected to two separate Tygon tubing II (Cole Parmer Tygon tubing AAD02091-CP, 0.010/0.030 inches inner/outer diameter) before sealing all channels with epoxy. To enable buffer exchange, Tygon tube I was connected to a syringe pump while Tygon tubes II were inserted into a buffer reservoir. Using a syringe pump, existing buffer was pulled from the side channels at a flow rate of 5 μl min^{-1} as new buffer from the reservoir was pulled in, thereby enabling diffusion-controlled buffer exchange into the central channel. Complete buffer exchange was achieved in 6–7 min. For disassembly measurements, the sample was initially in F-buffer before exchange to G-buffer, and *vice versa* for reassembly.

B Mathematical model

Master equations for filament length

Assuming that the filaments depolymerize independent of each other, the Master equation for filament length during disassembly is:

$$\frac{\mathrm{d}P(L,t)}{\mathrm{d}t} = k_{-}[P(L+1,t) - P(L,t)], \tag{1}$$

where $P(L,t)$ is the probability that a filament has length L in units of monomers at time t, and k_{-} is the rate of depolymerization. We assume that the polymerization rate is negligibly small during this stage. The Master equation for filament reassembly,[15,35–38] on the other hand, is more complex, and includes an initial nucleation stage, followed by a more favorable elongation stage. To account for this, we base our Master equation on the five-stage nucleation–elongation model proposed by Sept, Pollard and others.[15] We assume that at the beginning of reassembly, actin is present in the form of monomers only. Throughout the reassembly process polymerization takes place at a rate $k_{+}m(t)$, which, is directly proportional to the concentration of free actin monomers $m(t)$ present at any given time given the finite monomer pool. The rate of depolymerization k_{-}, however, depends on the stage of reassembly as in ref. 15 The Master equation is now given by:

$$\begin{aligned}\frac{\mathrm{d}P(L,t)}{\mathrm{d}t} &= k_{+}m(t)[P(L-1,t) - P(L,t)] \\ &\quad + [k_{-L}P(L+1,t) - k_{-L-1}P(L,t)],\end{aligned} \tag{2}$$

where the polymer length L is measured in units of monomers. We assume the rate of depolymerization of a dimer, k_{-1}, to be of the same order of magnitude as the polymerization rate k_{+}, and the rates for the next larger oligomers, k_{-2}, k_{-3}, and k_{-4}, are assumed to be progressively smaller. The rates k_{+}, k_{-3}, k_{-4}, and $k_{-\geq 5}$ are set to 10 $\mu\mathrm{M}^{-1}$ s^{-1}, 10 s^{-1}, 0 s^{-1}, and 1 s^{-1} respectively,

as in ref. 13. We set k_{-1} to 100 s^{-1} and varied k_{-2} from 10 s^{-1} to 100 s^{-1}. The concentration of actin monomers at a time t is given by $m(t) = P(1,t)m(0)$, $m(0)$ being the concentration of monomers in the system at the beginning of reassembly. By solving the above Master equations, we obtain the probability $P(L,t)$ during filament disassembly and reassembly, and calculate the average filament length $\langle L\rangle = \Sigma LP(L,t)$ at a given time t. To convert filament length from monomers to microns, we assume that each monomer is 2.7 nm long.

Effective medium theory of rigidity percolation

The model makes the following assumptions: (i) the F-actin network is approximated by a disordered hexagonal lattice whose mechanical properties are isotropic,[39–42] where every node is a freely rotating crosslink, every continuous series of collinear bonds constitute a fiber, and disorder is introduced by randomly removing bonds between nodes with probability $1 - p$, where $0 \leq p \leq 1$. The parameter p is the fraction of bonds that are present in the network, and is often called the bond occupation probability. The removal of bonds produces a broad distribution of fiber lengths, consistent with qualitative observations of *in vitro* F-actin networks. The fiber crosslinking occurs at lattice nodes homogeneously spaced by a minimum distance l_c, and has a concentration proportional to fiber density. (ii) Actin filaments are modeled as semiflexible filaments with constant stretching modulus, α, and bending modulus, κ. Defining r_{ij} to be the unit vector along bond ij, u_i as the displacement of the ith lattice site, and $u_{ij} = u_i - u_j$ as the displacement field, the deformation energy of the network is given by ref. 37.

$$E = \frac{\alpha}{2}\sum_{\langle ij\rangle} p_{ij}\left(u_{ij}\cdot\hat{r}_{ij}\right)^2 + \frac{\kappa}{2}\sum_{\langle ijk\rangle} p_{ij}p_{jk}\left[\left(u_{ji}+u_{jk}\right)\times\hat{r}_{ji}\right]^2. \quad (3)$$

Here, p_{ij} is 1 if bond ij is occupied and 0 otherwise, $\sum_{\langle ij\rangle}$ represents sum over all bonds, and $\sum_{\langle ijk\rangle}$ represents the sum over pairs of collinear bonds sharing a node. The first term is the cost of bond extension or compression, and is proportional to the fiber stretching modulus α. In terms of the Young's modulus Y, radius r, and crosslinking length l_c, we have $\alpha \sim Yr^2/l_c$. The second term arises from bending about the node connecting collinear bonds ij and jk, and is proportional to the scaled bending rigidity $\kappa \sim Yr^4/l_c^3$. The storage modulus of the network G' for a given average length $\langle L\rangle = l_c/(1-p)$, where p is the bond occupation probability of the network as defined earlier, was obtained by means of an effective medium theory calculation described in ref. 37 and 38. This calculation yields mechanical moduli of disordered networks for purely elastic response.

Acknowledgements

This research was funded by an NSF CAREER Award, grant number 1255446 to RMR-A, and Research Corporation & Gordon & Betty Moore Foundation Collaborative Innovation Award to RMR-A and JLR. MD and NB were partially supported by a Cottrell College Science Award from Research Corporation. MD further acknowledges the hospitality of the Aspen Center for Physics.

References

1 J. Stricker, T. Falzone and M. L. Gardel, *J. Biomech.*, 2010, **43**, 9–14.
2 Q. Wen and P. A. Janmey, *Curr. Opin. Solid State Mater. Sci.*, 2011, **15**, 177–182.
3 M. L. Gardel, K. E. Kasza, C. P. Brangwynne, J. Liu and D. A. Weitz, *Methods Cell Biol.*, 2008, **89**, 487–519.
4 G. M. Cooper and D. Ganem, *Nat. Med.*, 1997, **3**, 1042.
5 K. M. Schultz, A. D. Baldwin, K. L. Kiick and E. M. Furst, *Macromolecules*, 2009, **42**, 5310–5316.
6 M. D. Wehrman, S. Lindberg and K. M. Schultz, *Soft Matter*, 2016, **12**, 6463–6472.
7 J. H. Byrne, R. Heidelberger and M. N. Waxham, *From molecules to networks: an introduction to cellular and molecular neuroscience*, Academic Press, 2014.
8 O. Lieleg, M. Claessens, Y. Luan and A. Bausch, *Phys. Rev. Lett.*, 2008, **101**, 108101.
9 Y. Luan, O. Lieleg, B. Wagner and A. R. Bausch, *Biophys. J.*, 2008, **94**, 688–693.
10 T. D. Pollard, *J. Cell Biol.*, 1986, **103**, 2747–2754.
11 A. Jégou, T. Niedermayer, J. Orbán, D. Didry, R. Lipowsky, M.-F. Carlier and G. Romet-Lemonne, *PLoS Biol.*, 2011, **9**, e1001161.
12 A. H. Crevenna, M. Arciniega, A. Dupont, N. Mizuno, K. Kowalska, O. F. Lange, R. Wedlich-Söldner and D. C. Lamb, *eLife*, 2015, **4**, e04599.
13 I. Fujiwara, D. Vavylonis and T. D. Pollard, *Proc. Natl. Acad. Sci. U. S. A.*, 2007, **104**, 8827–8832.
14 I. Fujiwara, S. Takahashi, H. Tadakuma, T. Funatsu and S. Ishiwata, *Nat. Cell Biol.*, 2002, **4**, 666–673.
15 D. Sept, J. Xu, T. D. Pollard and J. A. McCammon, *Biophys. J.*, 1999, **77**, 2911–2919.
16 E. B. Stukalin and A. B. Kolomeisky, *Biophys. J.*, 2006, **90**, 2673–2685.
17 L. Mohapatra, T. J. Lagny, D. Harbage, P. R. Jelenkovic and J. Kondev, *Cell Syst.*, 2017, **4**, 559–567.
18 R. Tellam, *Biochemistry*, 1985, **24**, 4455–4460.
19 L. Blanchoin and T. D. Pollard, *Biochemistry*, 2002, **41**, 597–602.
20 L. S. Tobacman and E. D. Korn, *J. Biol. Chem.*, 1983, **258**, 3207–3214.
21 X. Li, J. Kierfeld and R. Lipowsky, *Phys. Rev. Lett.*, 2009, **103**, 048102.
22 H. Y. Kueh, W. M. Brieher and T. J. Mitchison, *Proc. Natl. Acad. Sci. U. S. A.*, 2008, **105**, 16531–16536.
23 P. A. Janmey, S. Hvidt, J. Käs, D. Lerche, A. Maggs, E. Sackmann, M. Schliwa and T. P. Stossel, *J. Biol. Chem.*, 1994, **269**, 32503–32513.
24 K. S. Zaner, *Biophys. J.*, 1995, **68**, 1019–1026.
25 J. Xu, A. Palmer and D. Wirtz, *Macromolecules*, 1998, **31**, 6486–6492.

26 F. Ziemann, J. Rädler and E. Sackmann, *Biophys. J.*, 1994, **66**, 2210–2216.
27 E. Frey, K. Kroy and J. Wilhelm, *Adv. Struct. Biol.*, 1999, **5**, 135–168.
28 R. Brau, J. Ferrer, H. Lee, C. Castro, B. Tam, P. Tarsa, P. Matsudaira, M. Boyce, R. Kamm and M. Lang, *J. Opt. A: Pure Appl. Opt.*, 2007, **9**, S103.
29 H. Lee, J. M. Ferrer, F. Nakamura, M. J. Lang and R. D. Kamm, *Acta Biomater.*, 2010, **6**, 1207–1218.
30 D. C. Morse, *Phys. Rev. E: Stat. Phys., Plasmas, Fluids, Relat. Interdiscip. Top.*, 1998, **58**, R1237.
31 F. G. Schmidt, B. Hinner and E. Sackmann, *Phys. Rev. E: Stat. Phys., Plasmas, Fluids, Relat. Interdiscip. Top.*, 2000, **61**, 5646.
32 G. M. Kavanagh and S. B. Ross-Murphy, *Prog. Polym. Sci.*, 1998, **23**, 533–562.
33 M. Gardel, M. Valentine, J. C. Crocker, A. Bausch and D. Weitz, *Phys. Rev. Lett.*, 2003, **91**, 158302.
34 S. Deshpande and T. Pfohl, *PLoS One*, 2015, **10**, e0116521.
35 F. Oosawa, S. Asakura *et al.*, *Thermodynamics of the Polymerization of Protein*, Academic Press, 1975.
36 L. Mohapatra, B. L. Goode, P. Jelenkovic, R. Phillips and J. Kondev, *Annu. Rev. Biophys.*, 2016, **45**, 85–116.
37 L. S. Tobacman and E. D. Korn, *J. Biol. Chem.*, 1983, **258**, 3207–3214.
38 T. C. T. Michaels and T. P. J. Knowles, *Am. J. Phys.*, 2014, **82**, 476–483.
39 M. Das, F. C. Mackintosh and A. J. Levine, *Phys. Rev. Lett.*, 2007, **99**, 038101.
40 M. Das, D. A. Quint and J. M. Schwarz, *PLoS One*, 2012, **7**, e35939.
41 J. L. Silverberg, A. R. Barrett, M. Das, P. B. Petersen, L. J. Bonassar and I. Cohen, *Biophys. J.*, 2014, **107**, 1721–1730.
42 C. Broedersz, X. Mao, T. Lubensky and F. C. MacKintosh, *Nat. Phys.*, 2011, **7**, 983–988.
43 B. Gurmessa, S. Ricketts and R. M. Robertson-Anderson, *Biophys. J.*, 2017, **113**, 1540–1550.
44 B. Gurmessa, R. Fitzpatrick, T. T. Falzone and R. M. Robertson-Anderson, *Macromolecules*, 2016, **49**, 3948–3955.
45 T. T. Falzone, S. Blair and R. M. Robertson-Anderson, *Soft Matter*, 2015, **11**, 4418–4423.
46 S. N. Ricketts, J. L. Ross and R. M. Robertson-Anderson, *Biophys. J.*, 2018, **115**, 1055–1067.
47 H. Isambert and A. Maggs, *Macromolecules*, 1996, **29**, 1036–1040.
48 M. Valentine, Z. Perlman, M. Gardel, J. Shin, P. Matsudaira, T. Mitchison and D. Weitz, *Biophys. J.*, 2004, **86**, 4004–4014.
49 R. M. Robertson-Anderson, *Optical Tweezers Microrheology: From the Basics to Advanced Techniques and Applications*, 2018.
50 C. D. Chapman, K. Lee, D. Henze, D. E. Smith and R. M. Robertson-Anderson, *Macromolecules*, 2014, **47**, 1181–1186.
51 C.-Y. Park, D. R. Jacobson, D. T. Nguyen, S. Willardson and O. A. Saleh, *Rev. Sci. Instrum.*, 2016, **87**, 014301.
52 D. T. Nguyen and O. A. Saleh, *Soft Matter*, 2017, **13**, 5421–5427.
53 M. C. Williams, *Biophysics Textbook Online*, http://www.biophysics.org/btol, 2002.
54 W. Weigand, A. Messmore, J. Tu, A. Morales-Sanz, D. Blair, D. Deheyn, J. Urbach and R. Robertson-Anderson, *PLoS One*, 2017, **12**, e0176732.
55 S. Burlacu, P. Janmey and J. Borejdo, *Am. J. Physiol. Cell Physiol.*, 1992, **262**, C569–C577.
56 E. D. Goley and M. D. Welch, *Nat. Rev. Mol. Cell Biol.*, 2006, **7**, 713–726.
57 E. Kaneshiro, *Cell Physiology Source Book: Essentials of Membrane Biophysics*, Academic Press, 2011.
58 W. Jung, M. P. Murrell and T. Kim, *ACS Macro Lett.*, 2016, **5**, 641–645.
59 S. Majumdar, L. C. Foucard, A. J. Levine and M. L. Gardel, arXiv preprint arXiv:1706.05336, 2017.
60 B. Schnurr, F. Gittes, F. MacKintosh and C. Schmidt, *Macromolecules*, 1997, **30**, 7781–7792.
61 D. H. Wachsstock, W. Schwarz and T. Pollard, *Biophys. J.*, 1994, **66**, 801–809.
62 T. D. Pollard and J. A. Cooper, *Science*, 2009, **326**, 1208–1212.
63 O. D. Weiner, G. Servant, M. D. Welch, T. J. Mitchison, J. W. Sedat and H. R. Bourne, *Nat. Cell Biol.*, 1999, **1**, 75.